UCLA
UCLA Previously Published Works

Title
Self-Assembly Strategy for Fabricating Connected Graphene Nanoribbons

Permalink
https://escholarship.org/uc/item/1t5467b1

Journal
ACS Nano, 9(12)

ISSN
1936-0851

Authors
Han, Patrick
Akagi, Kazuto
Federici Canova, Filippo
et al.

Publication Date
2015-12-22

DOI
10.1021/acsnano.5b04879

Peer reviewed

eScholarship.org Powered by the California Digital Library
University of California

Self-Assembly Strategy for Fabricating Connected Graphene Nanoribbons

Patrick Han,[*,†,‡] Kazuto Akagi,[†] Filippo Federici Canova,[§] Ryota Shimizu,[†] Hiroyuki Oguchi,[∥] Susumu Shiraki,[†] Paul S. Weiss,[†,‡] Naoki Asao,[*,†] and Taro Hitosugi[†]

[†]Advanced Institute for Materials Research (AIMR), Tohoku University, Sendai 980-8577, Japan, [‡]California NanoSystems Institute and Departments of Chemistry and Biochemistry and Materials Science and Engineering, University of California, Los Angeles, Los Angeles, California 90095, United States, [§]Aalto Science Institute, School of Science, Aalto University, 02150 Espoo, Finland, and [∥]Micro System Integration Center (μSIC) and Department of Nanomechamics, Tohoku University, Sendai 980-0879, Japan

ABSTRACT We use self-assembly to fabricate and to connect precise graphene nanoribbons end to end. Combining scanning tunneling microscopy, Raman spectroscopy, and density functional theory, we characterize the chemical and electronic aspects of the interconnections between ribbons. We demonstrate how the substrate effects of our self-assembly can be exploited to fabricate graphene structures connected to desired electrodes.

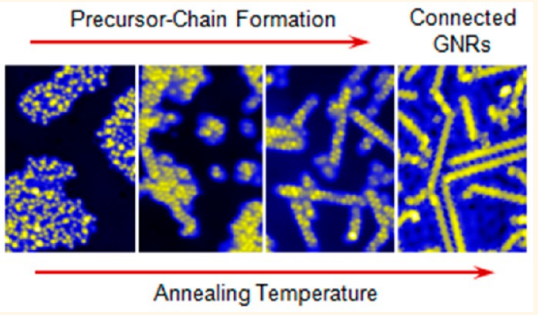

KEYWORDS: graphene nanoribbons · surface-assisted molecular assembly · bottom-up fabrication · scanning tunneling microscopy · graphene interconnections

Graphene promises to be a revolutionary material only if its honeycomb structure can be tailored and connected, both to engender desired properties from the nanoscopic scale and to enable property access from the macroscopic scale.[1,2] Conceptually, this control can be achieved by cutting graphene sheets into atomically precise graphene nanoribbons (GNRs):[3−18] reduced GNR widths induce applicative properties (such as switchable band gaps[6] or spin-polarized edges[4,5]), while the connections of GNRs lengthwise provide access to extraordinary electronic and other properties. However, current graphene-processing techniques cannot fulfill both conditions simultaneously,[19−21] producing either connected GNRs with unquantifiable defects[22−24] or defect-free GNRs in entangled bundles[10−17] that require additional isolation/connection processing.[18]

Here, we demonstrate surface-assisted molecular assembly (SAMA) that not only produces precise GNRs[7] but also connects these structures end to end—both chemically and electronically. Combining scanning tunneling microscopy (STM), Raman spectroscopy, and density functional theory (DFT), we found that the Cu{111} substrate guides precursor molecules to form and to connect (3,1)-chiral-edge GNRs up to 50 nm long, with both localized zigzag-edge states and delocalized π-states. We also found that π-delocalization is continuous throughout connected GNRs, indicating electronic connections. By connecting a precise GNR to other GNRs, we demonstrate that self-assembly can overcome the limitations of known graphene-processing methods, making this bottom-up process a potent strategy for fabricating and connecting precise graphene structures to desired electrodes. Our work indicates that, in addition to the width and edge configurations of the product GNRs,[12−14,25] future bottom-up GNR fabrication studies should also exploit both substrate effects[7,16,26] to control precursor alignments and polymerization chemistries[25,27−29] to functionalize target electrodes for GNR connection. We anticipate that this field will rapidly progress toward the inclusion of top-down methods to fabricate designer electrode platforms,[27,30−32] on which GNRs can be self-assembled, connected, and characterized.

* Address correspondence to pxh@wpi-aimr.tohoku.ac.jp, asao@m.tohoku.ac.jp.

Received for review August 5, 2015 and accepted November 13, 2015.

Published online November 20, 2015
10.1021/acsnano.5b04879

© 2015 American Chemical Society

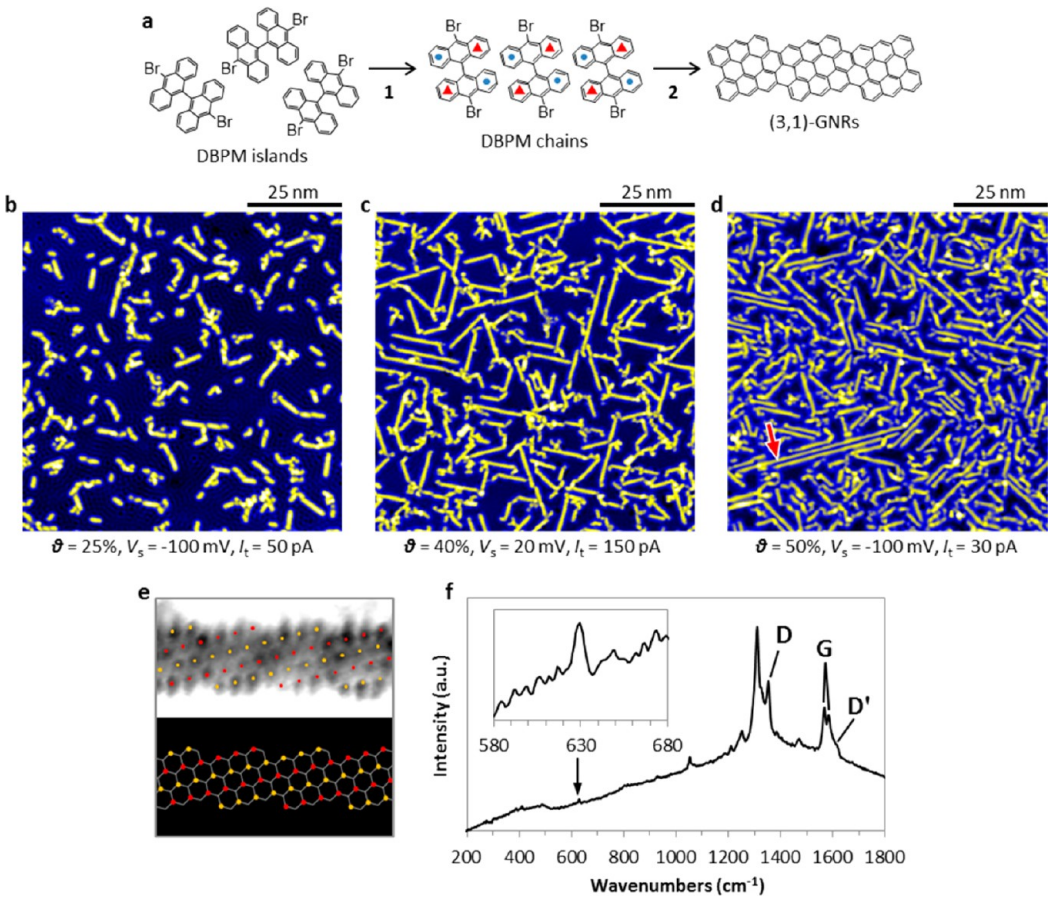

Figure 1. Fabricating chiral-edge graphene nanoribbons by self-assembly. (a) Scheme showing the two-step substrate-assisted molecular assembly of DBPM used to produce (3,1)-GNRs. The blue circles (red triangles) indicate molecular regions pointing toward (away from) the Cu{111} substrate. (b–d) Topographic scanning tunneling microscopy images (all with the same *xy* scale) showing the (3,1)-GNR length dependence on DBPM deposition coverage θ. The red arrow in (d) points to a ~50 nm long GNR. (e) Atomic structure of a section of a (3,1)-GNR. The top panel shows the high-resolution STM topographic image. The red and yellow dots highlight the α-carbons. The bottom panel shows the corresponding stick model. (f) Raman spectrum (532 nm) of (3,1)-GNR on Cu{111}. The G-band is split into two peaks at 1568 and 1583 cm^{-1}. The D′-band is observed as a shoulder near 1620 cm^{-1}. The D-band (1353 cm^{-1}) is accompanied by two peaks at 1310 and 1324 cm^{-1}. The inset of (f) shows the detail of the Raman signal at 629 cm^{-1} (black arrow), believed to be the out-of-plane zigzag-edge-localized mode.[36]

RESULTS AND DISCUSSION

To fabricate and to connect precise (3,1)-GNRs, we use the two-step thermally induced SAMA of 10,10′-dibromo-9,9′-bianthryl precursor monomers (DBPMs) on Cu{111} (Figure 1a),[7,8] exploiting both the strong interaction of Cu{111} with aromatic structures[33] to direct DBPM alignment and the stability of the C–Br bond to prevent unwanted reactions along GNR edges. As the scheme in Figure 1a depicts, this process involves the formation of DBPM molecular chains from DBPM molecular islands (1), followed by polymerization of the molecular chains (2). This latter step combines debromination of individual DBPMs and cyclodehydrogenation (CDH)[34] between DBPMs. By controlling the DBPM deposition coverage, θ (Figure 1b–d), and the speed of the annealing process (Supporting Information Figure S1), we can produce (3,1)-GNRs up to 50 nm long (Figure 1d, red arrow). The atomically resolved STM image of a GNR section in Figure 1e confirms the (3,1)-chiral-edge structure of our reaction product. As the histogram in Supporting Information Figure S2a shows, six preferred azimuthal GNR growth directions are observed, attributed to the alignment of the DBPM by Cu{111} during process 1.[7] This growth direction trend indicates that GNRs along the same growth direction are exclusively of the same adsorption chirality; it also indicates that the honeycomb crystalline structures of all product GNRs are directionally in phase (Supporting Information Figure S2b). Moreover, the presence of the DBPM Br atoms until the late stage of the GNR formation (process 2 in Figure 1a) prevents random C–C bond formation along the length of the GNR, promoting, instead, chemical connections exclusively between the molecular chain termini.

The Raman spectra of the chiral (3,1)-GNRs exhibit characteristics from both zigzag- and armchair-edge GNRs (Figure 1f). The G-band is split into two peaks (1568 and 1583 cm^{-1}), indicating the presence of narrow zigzag-edge GNR regions. According to the

interpretation of previous Raman investigations on the G-band splitting of zigzag-edge GNRs,[35] our observations indicate that the zigzag-edge C atoms of the (3,1)-GNRs are likely H-terminated, with Raman resonant frequencies lower than those for the non-edge C atoms. The inset of Figure 1f shows the details of a Raman signal at 629 cm^{-1} (black arrow) that is in excellent agreement with the out-of-plane edge-localized C–H mode, predicted for zigzag-edge GNRs.[36] Near the D-band (1353 cm^{-1}), two peaks are observed at 1310 and 1324 cm^{-1}. These peaks are likely the edge-phonon modes of the (3,1)-GNRs, activated by the armchair-edge regions.[17] The D′-band is observed as a shoulder near 1620 cm^{-1} and may indicate specific defects such as the pentagon–heptagon dislocations (topological defects).[18,37] While several other signals (1052, 1211, 1255, and 1470 cm^{-1}) still require theoretical interpretation, the Raman signature in Figure 1f unambiguously distinguishes (3,1)-GNRs from the armchair-edge GNRs previously observed on Au{111} and Ag{111}.[10,17]

Next, we use STM to test if SAMA can connect (3,1)-GNRs *via* two processes: "merging" DBPM chains and "molecular welding" of DBPM chains. We begin with the merging process, which we define as the convergence of the tips of growing DBPM chains at high θ, producing elbow GNR structures upon polymerization. Such elbow structures are observed in Figure 2a as the connections between straight (3,1)-GNRs. Highlighting the (3,1)-GNR-edge configurations, the colored brackets in Figure 2a indicate that GNRs of either the same adsorption chirality (GNRs 1 and 2) or the opposite adsorption chiralities (GNRs 3 and 4) can interconnect, forming elbow structures. Because the honeycomb structures of all (3,1)-GNRs are directionally in phase,[7] we expect the π-conjugation resulting from GNR interconnections to extend through the elbow—providing electronic continuity between both GNRs. Moreover, Figure 2a shows no evidence for CDH reaction occurring along the GNR edges, such as fusion between neighboring, parallel GNRs, nor the connection of a GNR terminus to the long edge of another GNR, as previously observed on the DBPM/Au{111} system.[18] Instead, every connection in Figure 2a is observed as an elbow structure, indicating that only the molecular chain termini are reactive. These results demonstrate that the SAMA in this work can be used to connect (3,1)-GNRs to other graphene structures, provided that their edges can undergo CDH (*e.g.*, GNR 4 is connected to GNRs 3 and 5).

Further, Figure 2a shows two types of apparent height modulations in STM images of (3,1)-GNRs. A low-frequency modulation is exemplified on GNR 6 as a gradual height increase, left to right, as displayed, across the entire GNR. Observed for longer GNRs, we posit that this modulation is caused by the lattice mismatch between the Cu{111} and the graphene

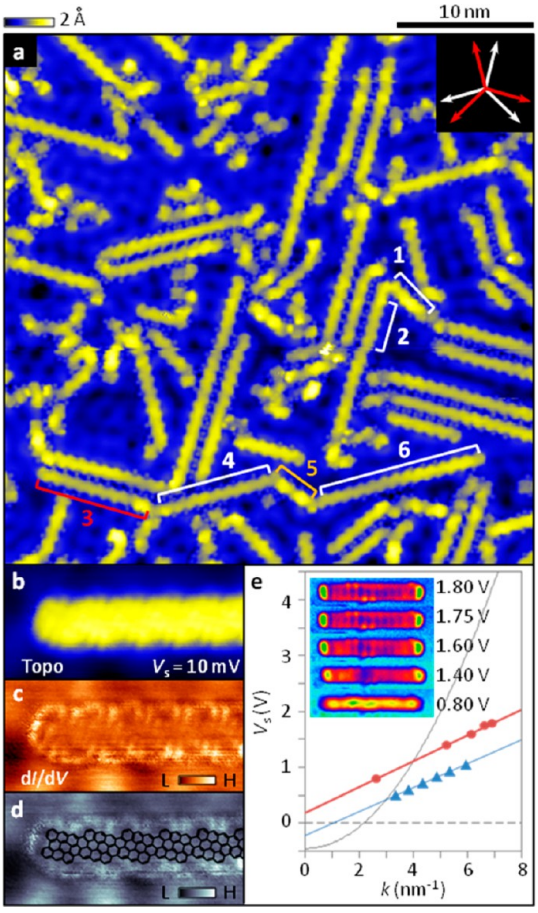

Figure 2. Connected graphene nanoribbons with zigzag-edge features and delocalized π-states. (a) Topographic STM image (V_s = 20 mV, I_t = 300 pA, θ = 50%) showing (3,1)-GNR interconnections on Cu{111}. The colored arrows in the top-right inset indicate the (3,1)-GNR growth directions, and red and white color-coded adsorption chiralities are within the brackets in the mainframe. (b) Topographic STM image (V_s = 10 mV, I_t = 350 pA) of a section of a GNR. (c) Differential conductance image (V_s = 10 mV, I_t = 350 pA) acquired simultaneously with (b). (d) Stick model overlaid on the same image as in (c). (e) Red dots in the mainframe show *k* measured from the d*I*/d*V* images of the 14 monomer long GNR in the inset (also see Figure 3). The red linear fit intersects the *y*-axis at *V* = 0.189 eV. The blue triangles in (e) show *k* measured from the free-standing model of the same GNR (Supporting Information Figure S6). The gray parabola in (e) shows *E*(*k*) for the Cu{111} surface state.

honeycomb, resulting in long-range apparent height modulations, similar to the Moiré patterns observed over epitaxial graphene on Cu{111}.[38] A second, short-distance modulation is exemplified on GNR 3 as a one DBPM wide height protrusion near the connection with GNR 4. We attribute this modulation to a slight translational phase shift between GNRs 3 and 4, also caused by the Cu{111}/graphene lattice mismatch. We propose that, upon polymerization connecting GNRs 3 and 4, the honeycomb translational phase shift introduces mechanical strain near the elbow junction, explaining the observed height protrusions.

Beside the merging process, Figure 2a also shows evidence that stray DBPM molecules can connect

growing DBPM chains; a process we define as molecular welding. In Figure 2a, GNR 5 exhibits a pair of one DBPM wide protrusions. However, as bracket 5 illustrates, the growth direction of GNR 5 is unexpected, lying between that of GNRs 1 and 3. This observation suggests that GNR 5 does not originate from the DBPM chain formation depicted in Figure 1a. We propose that GNR 5 is formed by several (with the exact number unclear) DBPMs caught between GNRs 4 and 6 during chain formation, where these trapped DBPMs interact not only with Cu{111} but also with the extremities of the DBPM chains of GNRs 4 and 6 already formed. This unusual environment causes the DBPMs to misalign—even to undergo rearrangement of C atoms—as the GNRs interconnect.[18,28] In effect, upon polymerization, the stray DBPM molecules weld GNRs 4 and 6 together, forming two elbow junctions. We note that, for both merging and molecular welding processes, the determination of the exact connection chemistry remains challenging because the atomic structures of the resulting elbow connections are difficult to resolve using STM. As Supporting Information Figure S3 demonstrates, the chemical structure of many elbow junctions cannot be modeled with intact DBPM units straightforwardly. Later in this work, we will combine STM and DFT results to resolve the chemical structure of an elbow and to propose CDH as a possible connection mechanism.

Next, we use STM differential conductance (d*I*/d*V*) imaging[13,39−41] to investigate the electronic connection at the GNR elbow structures. We find that (3,1)-GNRs exhibit both localized states at the zigzag-edge regions and delocalized π-states along the lengths of the GNRs. We also combine d*I*/d*V* imaging with DFT modeling to test if π-delocalization extends through elbow junctions, connecting GNRs electronically, which it does. Figure 2b,c shows the simultaneously acquired STM topographic and d*I*/d*V* images of a (3,1)-GNR section, respectively. Near the Fermi energy (E_F) (sample bias $V_s = +10$ mV), the GNR local density of states (LDOS) is modulated along the (3,1)-chiral edges (Figure 2c). As the stick model in Figure 2d highlights, LDOS enhancements near the zigzag regions are observed as protrusions in these d*I*/d*V* images. These features indicate that zigzag regions have higher densities of empty states compared to the non-zigzag regions. The armchair tip of the GNR in Figure 2c also shows enhanced LDOS compared with the medial line of the ribbon, as was previously observed for armchair GNRs.[13] We propose that the empty states observed at the zigzag-edge regions originate from the GNR π-band edge,[5] caused by negative charge transfer from the GNR to the Cu{111}. The observation of this charge transfer is discussed next.

When imaged at higher sample bias voltages (0.8 V ≤ V_s ≤ 1.8 V, Figure 2e), (3,1)-GNRs exhibit periodic modulations along the medial line of the ribbons. As the

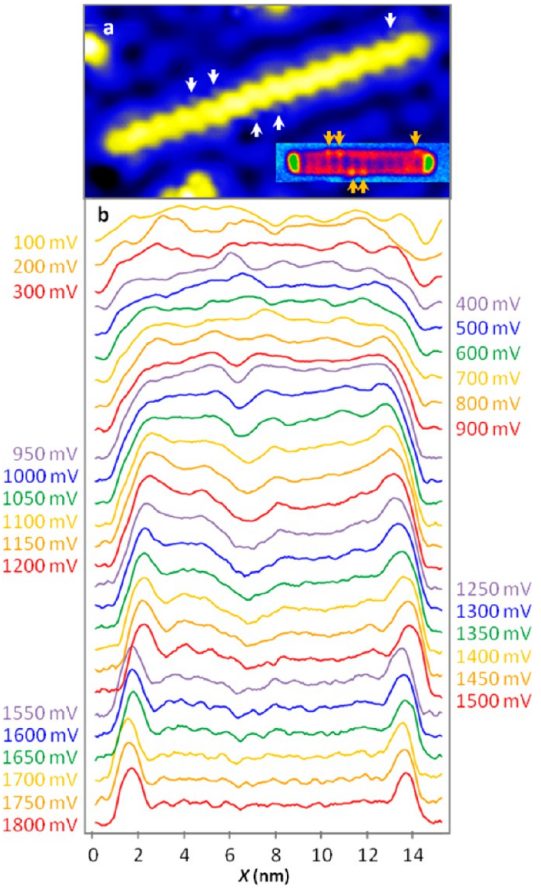

Figure 3. Delocalized, quantum-confined graphene-nanoribbon electronic states. (a) Topographic scanning tunneling microscopy image showing a 14 monomer long (3,1)-GNR and its local environment. Each of the four white arrows points to a free Br atom. The inset of (a) shows the differential conductance (d*I*/d*V*) image of the same GNR acquired at V_s = 1800 mV. The four orange arrows point to the Br atoms mentioned above. The GNR imaged in (a) is the same structure imaged in the inset of Figure 2e. (b) Colored traces show profiles of d*I*/d*V* images (not shown) acquired on the 14 monomer long GNR from (a). The vertical axis shows d*I*/d*V* (arbitrary units). The colored numbers indicate V_s of the corresponding curve. The d*I*/d*V* profiles in (b) are modulated by a feature at *x* = 6 nm (*i.e.*, between the two arrow pairs in (a); also, see inset of Figure 2e). Because this feature is not observed in the topographic image, we propose that it is a substrate defect, possibly a missing Cu atom underneath the GNR.

Figure 2e inset and Figure 3 both show, the modulation period λ of a 14 DBPM long GNR increases with decreasing V_s—a hallmark of 1D and 2D free-electron systems, where spatial confinement only allows electrons of discrete energies.[40] While we could not isolate the eigenstates using d*I*/d*V* spectroscopy at the center of (3,1)-GNRs (Supporting Information Figure S4), we extract the energy dispersion curve *E*(*k*) from our measured λ, using wave vector $k = 2\pi/\lambda$ (red dots in Figure 2e and Supporting Information Figure S5). As the red curve fit in Figure 2e indicates, *E*(*k*) of the 14 DBPM long GNR is linear, with a slope comparable to *E*(*k*) calculated for a free-standing GNR of the same length (blue curve fit in Figure 2e and Supporting Information Figure S6). Reminiscent of the graphene Dirac cone, this

result implies that both the measured $E(k)$ (Figure 2e) and the observed d*I*/d*V* periodic modulations (Figure 2e inset) originate from the delocalized (3,1)-GNR π^*-band (Supporting Information Figure S7).[5] We attribute the ~0.2 V energy upshift of the measured $E(k)$ to the negative charge transfer from the GNR to the substrate, as was previously observed on graphene islands on Cu{111}.[42] As the DFT-calculated LDOS energy distribution in Figure 4 illustrates, this charge transfer shifts the (3,1)-GNR π-band edge (yellow arrow) up past E_F (black dashed line), rendering it observable by d*I*/d*V* imaging at $V_s = +10$ mV, most prominently at the GNR zigzag-edge regions (Figure 2c).

Further, the GNR tips and edges in Figures 2e and 3 show higher LDOS at higher energy levels. These protrusions, which stem from the phase shift of the standing waves at the GNR termini,[39] mark the disruption (*i.e.*, termination) of the π-conjugation. Similar LDOS protrusions are observed at elbow junctions formed by only one C−C bond (*i.e.*, no electronic connection, Figure 5). We combine d*I*/d*V* imaging and DFT modeling to demonstrate that π-conjugation remains continuous across elbow structures connected by at least four C−C bonds. Figure 6a compares the LDOS of an elbow connection with that of a single (3,1)-GNR (red arrows in bottom panel). As this comparison indicates, both GNR structures share the same electronic architecture. At $V_s = 1.8$ V, regions of high LDOS are located at the GNR tips and edges; regions of low LDOS are observed along the GNR medial lines, decorated by standing wave patterns.[26] At the elbow connection, the medial line of the graphene structure does not show LDOS enhancement (which would signal disrupted π-conjugation, Figure 5). This result suggests that, unlike the (3,1)-GNR tips, where π-conjugation terminates, the observed elbow connection acts as the medial line of a single (3,1)-GNR, supporting continuous π-conjugation (also see Supporting Information Figure S3b). We use DFT to model the LDOS of several chemical structures fitting the topographic images of the elbow near $E = 1.8$ V (Supporting Information Figure S8). Figure 6b,c shows the two most plausible structures, both with electronic features directly relatable to our d*I*/d*V* observations. The features at the GNR edges (displayed as green) indicate regions of enhanced LDOS caused by the presence of edge C−H bonds; modulations through the GNR medial line (displayed as cyan), originating from carbon p_z orbitals, indicate π^*-delocalization (Supporting Information Figure S7). Further, both structures in Figure 6b,c account for the apparent height modulation shown in the inset of Figure 6c, either by steric hindrance between neighboring H atoms (shown as the red spot

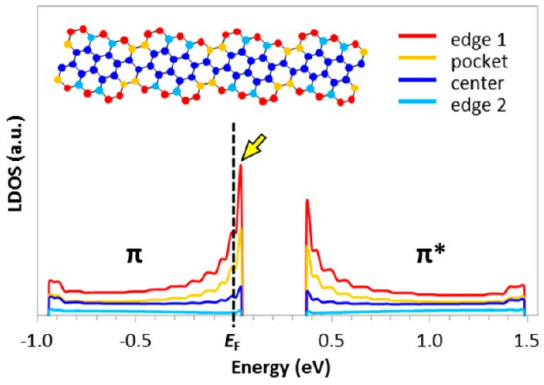

Figure 4. Density functional theory investigation of the zigzag-edge states. The bottom figure shows the calculated local density of states energy distributions for the π- and π^*-bands of the free-standing, infinite (3,1)-GNR for four types of C atom positions (legend and top-left structure). The black dashed line indicates the position of the Fermi energy caused by a ~0.2 V GNR-to-Cu{111} negative charge transfer. The yellow arrow highlights the π-band edge, *i.e.*, the electronic features imaged in Figure 2c. For this calculation, 27 × 15 × 15 *k*-points were used.

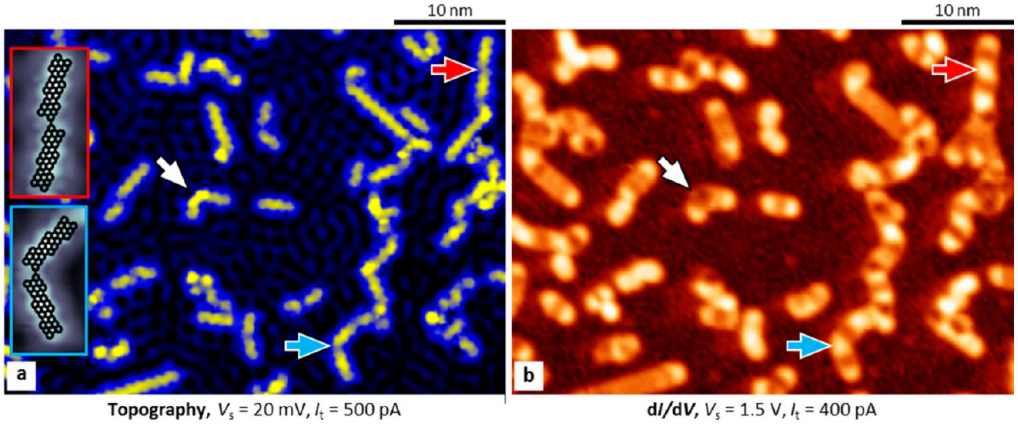

Figure 5. Testing the π-conjugation at elbow connections by spectroscopic imaging. (a,b) Scanning tunneling microscopy topographic and differential conductance images of the same (3,1)-GNR/Cu{111} area, respectively. The white arrows indicate GNR connection with continuous π-conjugation. The elbow of this structure appears as a depression in (b). The red and blue arrows indicate regions where π-conjugation is not continuous. The contact points of these structures appear as protrusions in (b). The insets in (a) show the stick models of the GNR meeting points indicated by the arrows of corresponding colors.

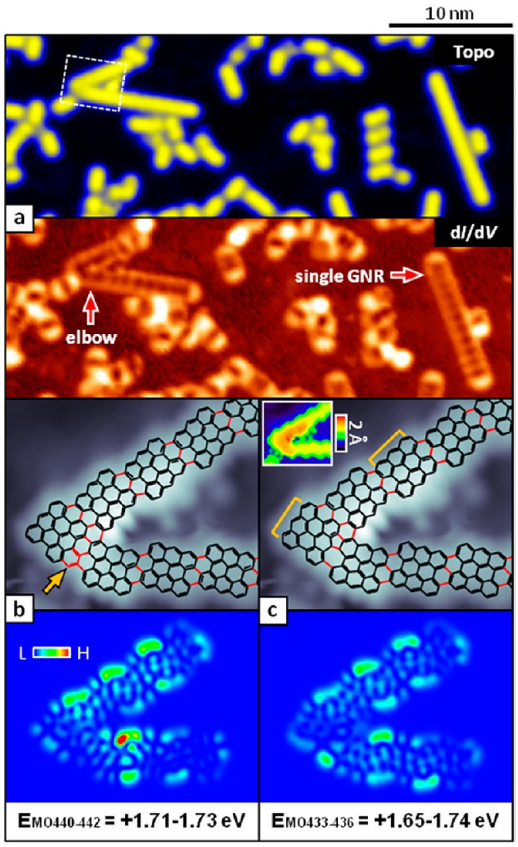

Figure 6. Self-assembled electronic connections. The top and bottom panels of (a) show the simultaneously acquired STM topographic (V_s = 1.8 V, I_t = 1 nA) and d*I*/d*V* images (V_s = 1.8 V, I_t = 1 nA) of a (3,1)-GNR/Cu{111} surface, respectively. The red arrows in the bottom panel of (a) compare the local density of states of a pair of connected GNRs (elbow) with that of a single GNR. The top and bottom panels of (b,c) show two proposed chemical structures (H atoms not shown) and the corresponding calculated electronic structures of the free-standing elbow, respectively. The black (red) lines in the top panels of (b,c) indicate DBPM units (bonds formed between DBPMs). The inset in (c) shows the same STM topographic image (V_s = 100 mV, I_t = 1 nA) as the images in the backgrounds of (b,c). The yellow arrow in (b) highlights three C atoms that are currently unaccounted. The yellow brackets in (c) highlight the angular misalignment between the honeycombs of the two DBPM units. This shift implies that the honeycomb near the elbow is misaligned with the Cu{111} lattice. The bottom numbers in (b,c) show the energy range for summation of the nearly degenerated molecular orbitals obtained from the corresponding density functional theory models.

in the bottom panel of Figure 6b) or by misalignment of the elbow honeycomb with the underlying Cu{111} lattice (shown by the yellow brackets in Figure 6c).

While we, thus far, have insufficient evidence to determine directly which model represents the observed elbow structure, both models support the continuity of π-conjugation at the elbow junction. However, the structure in Figure 6b includes three carbon atoms (yellow arrow), whose source cannot be explained straightforwardly. Moreover, recent noncontact atomic force microscopy (nc-AFM) results have shown that fusing graphene structures together *via* CDH often produces pentagon−heptagon (topological) defects where fusion occur,[18] supporting the structure in Figure 6c as plausible. This type of defect may also explain the observation of the D′-band in our Raman spectrum (Figure 1f). From this latter structure, we propose that one possible connection mechanism of (3,1)-GNRs on Cu{111} is CDH (Figure 7 and Supporting Information Figure S9). This is demonstrated by the red lines in Figure 7 (and Figure 6c), which highlight the C−C bonds formed by CDH both along the straight GNR and at the elbow connection. However, to confirm that CDH is the main connection mechanism, techniques such as nc-AFM may be required to resolve the structures exemplified by Supporting Information Figure S3. Only then can the proposed mechanism be determined.

Next, we test how the reactivity and the lattice structure of Cu{111} align DBPMs during self-assembly. We propose that these properties can be exploited to obtain desired GNR connections. Figure 8a−f shows a DBPM/Cu{111} surface (θ = 40%), obtained from a single deposition and sampled the annealing temperatures, T_a, shown for STM imaging at 5.6 K. From this image sequence, we deduce that the average molecular chain length is determined at the critical temperature range of 200 °C < T_a < 400 °C *via* molecular diffusion (see Supporting Information Figure S9 for proposed step-by-step assembly mechanism). When the annealing process at this temperature range is reduced for STM imaging, the average length of the product GNR is significantly reduced. We demonstrate this effect in Figure 9, which compares the length distributions of (3,1)-GNRs fabricated by the unperturbed annealing process shown in Supporting Information Figure 1 (pink bars), with that stopped at several T_a for STM imaging (green bars). We propose that a long (several hours, Supporting Information Figure S1), steady anneal at 200 °C < T_a < 400 °C and $\theta \leq$ 40% would allow DBPM diffusion to maximize the molecular chain length—therefore the product of GNR lengths. This capability, combined with factors such as Cu substrate step density,[16] will be extremely useful for connecting (3,1)-GNRs or other specific GNRs to desired contacting electrodes by SAMA.

CONCLUSIONS AND PROSPECTS

We have utilized specific features of the DBPM SAMA on Cu{111} (*i.e.*, pronounced interactions between Cu{111} and aromatic structures,[33] reduced number of growth directions, and C−Br bond stability[7]) to achieve simultaneous fabrication and interconnection of (3,1)-GNRs. We found that these substrate effects of Cu{111} guide DBPM chains to form graphene elbow structures, providing atomic-resolution evidence for exclusive end-to-end interconnections of GNRs. Further, our spectroscopic imaging showed evidence that the delocalization of the product GNR π-system is continuous over elbow junctions, indicating electronic

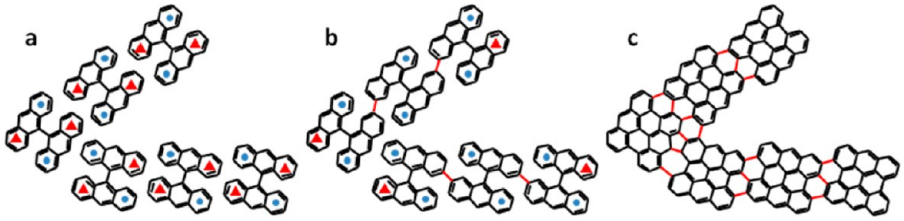

Figure 7. Graphene nanoribbon connection by cyclodehydrogenation. (a) Two precursor molecular chains in position to form the elbow structure shown in Figure 6c, aligned by Cu{111} upon thermal annealing. Blue dots (red triangles) indicate bianthryl regions pointing away (toward) the substrate. (b) Upon further annealing, regions pointing toward Cu{111} undergo the first stage of CDH, forming C−C bonds (redlines) with neighboring C atoms. Reacted regions are flattened out. (c) Further annealing induced second-stage CDH between regions pointing away from Cu{111}, forming C−C bonds between neighboring C atoms. The entire structure flattens into a graphene elbow structure. The exact order of individual C−C bond formation during stage two is not unclear. In this model, the elbow molecule is rotated by ~8° counterclockwise with respect to the midline of the top chain. Bromine and H-atoms are omitted for clarity.

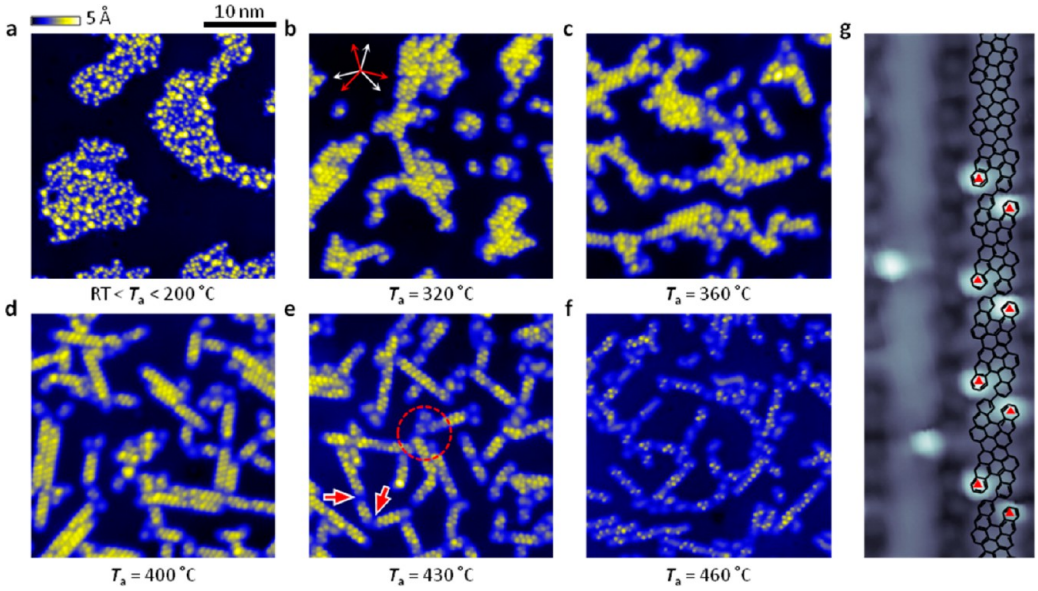

Figure 8. Substrate that assembles and connects graphene nanoribbons. (a−f) Topographic STM images (all presented with the same lateral and topographic scales) showing the DBPM/Cu{111} at various stages of thermal annealing. (a) Up to T_a = 200 °C, DBPM forms disordered molecular islands on Cu{111}. (b,c) At 320 °C ≤ T_a ≤ 360 °C, DBPM islands change shape *via* molecular diffusion, growing along preferred surface azimuthal directions (red and white arrows in (b)). In (b,c), rows of staggered protrusions—*i.e.*, the molecular chains depicted in Figure 1a—are discernible within islands. (d−f) For T_a ≥ 400 °C, STM images no longer show change in molecular chain lengths and dispersion; only CDH is observed as the gradual flattening of the staggered protrusions. Examples of merging molecular chains (red arrows) and molecular welding (red dashed circle) are exemplified in (e). (g) High-resolution STM topographic image (V_s = 100 mV, I_t = 30 pA) of a region near (f). The stick model in (g) illustrates regions of incomplete CDH reaction, imaged as protrusions (compare with Figure 1a).

connection between GNRs. In effect, we report a SAMA, whose mechanism provides the means to fabricate and to connect precise (3,1)-GNRs to desired graphene electrodes simultaneously—as long as these contacting electrodes are properly functionalized to undergo connective CDH.

The results from this work describe a bottom-up strategy for the fabrication of connected graphene nanostructures with a minimum amount of defects. Current bottom-up fabrication methods focus on preserving the polymerization chemistry of precursor molecules.[10−18] This is usually achieved either by solution chemistry[14,25,29] or by selecting inert substrates that do not perturb the GNR self-assembly chemistry (*e.g.*, Au{111}[10−16,18] or Ag{111}[17]). However, these approaches invariably produce GNR bundles that require additional isolation/connection processing—additional steps that introduce unpredictable reactions, notably along the GNR edges, and thus nonprecise reaction products.[18] Our work demonstrates that pronounced substrate effects need not be avoided but instead can be exploited to direct precursor polymerization reactions.

To this end, the DBPM/Cu{111} SAMA mechanism described here can be exploited to render the product (3,1)-GNRs accessible to the macroscopic scale *during* the assembly process. Figure 1b−d indicates that the average length of single, straight (3,1)-GNRs increases with DBPM coverage. However, the GNR average length is also limited by the six-direction growth mode: on the

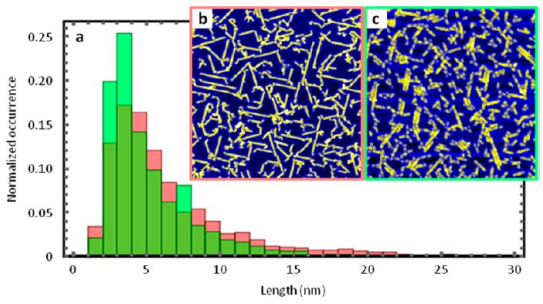

Figure 9. Graphene nanoribbon length dependence on annealing pathways. (a) Histogram comparing the GNR length resulting from two annealing processes. The pink bars show the GNR length distribution resulting from the annealing process shown in Supporting Information Figure S1. The green bars show the GNR length distribution resulting from an annealing process interrupted at T_a = 320, 360, 400, 430, and 460 °C for STM imaging at T_{STM} = 5.6 K. (b) Topographic STM image of the surface obtained by the normal annealing procedure. (c) Topographic STM image of the surface obtained by interrupted annealing. For both (b,c), θ = 40%.

flat Cu{111} surface, the formation of elbow connections terminates the growth of single GNRs. This problem can be avoided if the (3,1)-GNR growth mode is further reduced to a single direction, for example, using a high-Miller-index Cu surface,[16] whose atomic step edges are aligned with one of the six (3,1)-GNR growth directions. Combined with the controlled DBPM deposition coverage (Figure 1) and annealing procedure (Figure 8), one directional growth would imply that, during SAMA, merging DBPM chains form single, straight (3,1)-GNRs, multiplying ribbon lengths with each connection (as exemplified by the 50 nm long GNR in Figure 1d). Conceptually, this growth mode can produce defect-free (3,1)-GNRs in the micrometer scale, in a single direction.

To conclude, future SAMA design should explore the effects of reactive substrates with low carbon solubility[43] on precursor molecular self-assembly (*e.g.*, Ir{111}[40,41,44] and Pt{111}[45]). Elucidation of these substrate effects can then be combined with the precursor polymerization chemistry to produce GNRs of lengths accessible by top-down processes and desired edge configurations—including the elusive zigzag-edge GNRs. Further, as a strategy to isolate precise graphene structures from the substrate electronically, future SAMA design should also target insulator surface systems with substrate/precursor interactions that are strong enough to enable precursor alignment but weak enough to enable molecular chain formation *via* surface diffusion. Another direction for this strategy will target the fabrication/connection of single GNRs to distinct graphene electrodes and networks. This objective can first be achieved by the simultaneous deposition of different designed precursors, each designated for producing GNR device and graphene electrodes. Our work demonstrates that, by exploiting the substrate effects, SAMA is a potent strategy toward connecting the amazing properties of precise graphene structures to the macroscopic scale.

METHODS

Preparation, Scanning Tunneling Microscopy, and Raman Investigation of (3,1)-GNRs. Cu{111} single crystal (MaTecK GmbH, Jülich, Germany) was prepared by repeated cycles of Ar^+ ion bombardment and annealing at 500 °C and cooled down to room temperature (RT) for use as a substrate for GNR growth. The 10,10′-dibromo-9,9′-bianthryl precursor monomers (synthesized according to the method reported in ref 10) were deposited in ultrahigh vacuum by sublimation using a custom-made Knudsen cell at RT. For Figures 1−3, 5, and 6, polymerization was performed by annealing DBPM/Cu{111} at the temperature program shown in Supporting Information Figure S1, except when using STM to study the effects of selected annealing temperatures T_a on the morphology of the DBPM self-assembly (Figure 8). For Figure 8, the annealing process was started as in Supporting Information Figure S1 and was stopped when the annealing at the first T_a was completed. The sample was then transferred to the STM stage for imaging at 5.6 K. Following STM imaging, the sample was transferred back to the annealing stage and the annealing process was resumed from T_a up to the next temperature. Surface coverages were monitored by STM. All STM images were acquired using a custom-made STM[46,47] at 5.6 K and were processed with WSXM software.[48] We used commercial PtIr tips (P-100PtIr(S) series, Unisoku, Japan). We monitored T_a optically using an infrared pyrometer.[8] Our Cu sample (7 mm × 2 mm × 1 mm) was heated using a filament located at its backside.

The Raman measurements were performed using a Thermo Scientific Nicolet Almega-HD microscope with a Nd:YVO4 laser (532 nm). The (3,1)-GNR/Cu{111} sample was first transported from the STM using a vacuum suitcase to a glovebox, where it was exposed to an Ar atmosphere and placed inside a portable container equipped with a viewport. This container was then used for Raman measurements. The sample was never exposed to air.

Growth Direction Measurements, Image Processing, and Density Functional Theory Calculations. To compile the GNR growth direction histogram in Figure 1f, we measured the angles between the linear GNR structures observed in three STM images acquired over different areas of the surface represented by Figure 1d and the horizontal direction. We used the vector-based software Serif DrawPlus to isolate the GNRs from our STM topographs as straight lines, which are directly used for angle measurements.

Our calculations were done using the Vienna *ab-initio* simulation package (VASP) code,[49] with projector augmented wave method (PAW) potentials and Perdew−Burke−Ernzerhof exchange-correlation (PBE) functionals.[50] Structure optimizations were performed with an E_{cutoff} of 400 eV and Γ-point sampling. The LDOS density maps were visualized at the height of 3.0 Å. Further details are given in the Supporting Information.

Conflict of Interest: The authors declare no competing financial interest.

Supporting Information Available: The Supporting Information is available free of charge on the ACS Publications website at DOI: 10.1021/acsnano.5b04879.

Additional figures showing information on the annealing speed and temperature on the self-assembly process; effects of the Cu{111} substrate on GNR growth directions; additional structure assignments and d*I*/d*V* images of GNR elbow structures; calculated band structure and LDOS energy distribution of a free-standing, infinite (3,1)-GNR; additional d*I*/d*V* point spectra comparing different STM tips and GNRs of different lengths; details of DFT calculations of model elbow structures; comparisons of average GNR lengths with different annealing processes (PDF)

Acknowledgment. We thank T. Hanaguri for designing the STM scanner, K. Iwaya for setting up the STM system, S. Orimo for providing the Raman spectrometer, T. Sato for assisting us with the Raman measurements, and K. Kim for providing the fume hood. The computation in this work was performed using the HA8000 system of RIIT at Kyushu University. This work was supported by the World Premier Research Center Initiative (WPI), promoted by the Ministry of Education, Culture, Sports, Science and Technology (MEXT) of Japan.

REFERENCES AND NOTES

1. Novoselov, K. S.; Fal'ko, V. I.; Colombo, L.; Gellert, P. R.; Schwab, M. G.; Kim, K. A Roadmap for Graphene. *Nature* **2012**, *490*, 192–200.
2. Tour, J. M. Top-Down *versus* Bottom-Up Fabrication of Graphene-Based Electronics. *Chem. Mater.* **2014**, *26*, 163–171.
3. Yazyev, O. V. A Guide to the Design of Electronic Properties of Graphene Nanoribbons. *Acc. Chem. Res.* **2013**, *46*, 2319–2328.
4. Son, Y.-W.; Cohen, M. L.; Louie, S. G. Half-Metallic Graphene Nanoribbons. *Nature* **2006**, *444*, 347–349.
5. Yazyev, O. V.; Capaz, R. B.; Louie, S. G. Theory of Magnetic Edge States in Chiral Graphene Nanoribbons. *Phys. Rev. B: Condens. Matter Mater. Phys.* **2011**, *84*, 115406.
6. Son, Y.-W.; Cohen, M. L.; Louie, S. G. Energy Gaps in Graphene Nanoribbons. *Phys. Rev. Lett.* **2006**, *97*, 216803.
7. Han, P.; Akagi, K.; Federici Canova, F.; Mutoh, H.; Shiraki, S.; Iwaya, K.; Weiss, P. S.; Asao, N.; Hitosugi, T. Bottom-Up Graphene-Nanoribbon Fabrication Reveals Chiral Edges and Enantioselectivity. *ACS Nano* **2014**, *8*, 9181–9187.
8. Han, P.; Akagi, K.; Federici Canova, F.; Mutoh, H.; Shiraki, S.; Iwaya, K.; Weiss, P. S.; Asao, N.; Hitosugi, T. Reply to ″Comment on 'Bottom-Up Graphene-Nanoribbon Fabrication Reveals Chiral Edges and Enantioselectivity'″. *ACS Nano* **2015**, *9*, 3404–3405.
9. Simonov, K. A.; Vinogradov, N. A.; Vinogradov, A. S.; Generalov, A. V.; Zagrebina, E. M.; Mårtensson, N.; Cafolla, A. A.; Carpy, T.; Cunniffe, J. P.; Preobrajenski, A. B. Comment on ″Bottom-Up Graphene-Nanoribbon Fabrication Reveals Chiral Edges and Enantioselectivity″. *ACS Nano* **2015**, *9*, 3399–3403.
10. Cai, J.; Ruffieux, P.; Jaafar, R.; Bieri, M.; Braun, T.; Blankenburg, S.; Muoth, M.; Seitsonen, A. P.; Saleh, M.; Feng, X.; *et al.* Atomically Precise Bottom-Up Fabrication of Graphene Nanoribbons. *Nature* **2010**, *466*, 470–473.
11. Chen, Y.-C.; de Oteyza, D. G.; Pedramrazi, Z.; Chen, C.; Fischer, F. R.; Crommie, M. F. Tuning the Band Gap of Graphene Nanoribbons Synthesized from Molecular Precursors. *ACS Nano* **2013**, *7*, 6123–6128.
12. Cai, J.; Pignedoli, C. A.; Talirz, L.; Ruffieux, P.; Soede, H.; Liang, L.; Meunier, V.; Berger, R.; Li, R.; Feng, X.; *et al.* Graphene Nanoribbon Heterojunctions. *Nat. Nanotechnol.* **2014**, *9*, 896–900.
13. Chen, Y.-C.; Cao, T.; Chen, C.; Pedramrazi, Z.; Haberer, D.; de Oteyza, D. G.; Fischer, F. R.; Louie, S. G.; Crommie, M. F. Molecular Bandgap Engineering of Bottom-Up Synthesized Graphene Nanoribbon Heterojunctions. *Nat. Nanotechnol.* **2015**, *10*, 156–160.
14. Liu, J.; Li, B.-W.; Tan, Y.-Z.; Giannakopoulos, A.; Sanchez-Sanchez, C.; Beljonne, D.; Ruffieux, P.; Fasel, R.; Feng, X.; Muellen, K. Toward Cove-Edged Low Band Gap Graphene Nanoribbons. *J. Am. Chem. Soc.* **2015**, *137*, 6097–6103.
15. Tao, C. G.; Jiao, L. Y.; Yazyev, O. V.; Chen, Y. C.; Feng, J. J.; Zhang, X. W.; Capaz, R. B.; Tour, J. M.; Zettl, A.; Louie, S. G.; *et al.* Spatially Resolving Edge States of Chiral Graphene Nanoribbons. *Nat. Phys.* **2011**, *7*, 616–620.
16. Linden, S.; Zhong, D.; Timmer, A.; Aghdassi, N.; Franke, J. H.; Zhang, H.; Feng, X.; Müllen, K.; Fuchs, H.; Chi, L.; *et al.* Electronic Structure of Spatially Aligned Graphene Nanoribbons on Au(788). *Phys. Rev. Lett.* **2012**, *108*, 216801.
17. Huang, H.; Wei, D. C.; Sun, J. T.; Wong, S. L.; Feng, Y. P.; Castro Neto, A. H.; Wee, A. T. S. Spatially Resolved Electronic Structures of Atomically Precise Armchair Graphene Nanoribbons. *Sci. Rep.* **2012**, *2*, 00983.
18. Dienel, T.; Kawai, S.; Söde, H.; Feng, X.; Müllen, K.; Ruffieux, P.; Fasel, R.; Gröning, O. Resolving Atomic Connectivity in Graphene Nanostructure Junctions. *Nano Lett.* **2015**, *15*, 5185–5190.
19. Savage, N. Super Carbon. *Nature* **2012**, *483*, S30–S30.
20. Peplow, M. The Quest for Supercarbon. *Nature* **2013**, *503*, 327–329.
21. Colapinto, J. Material Question *The New Yorker* [Online], 2014, http://www.newyorker.com/magazine/2014/12/22/material-question.
22. Han, M. Y.; Brant, J. C.; Kim, P. Electron Transport in Disordered Graphene Nanoribbons. *Phys. Rev. Lett.* **2010**, *104*, 056801.
23. Sprinkle, M.; Ruan, M.; Hu, Y.; Hankinson, J.; Rubio-Roy, M.; Zhang, B.; Wu, X.; Berger, C.; de Heer, W. A. Scalable Templated Growth of Graphene Nanoribbons on SiC. *Nat. Nanotechnol.* **2010**, *5*, 727–731.
24. Li, Y. Y.; Chen, M. X.; Weinert, M.; Li, L. Direct Experimental Determination of Onset of Electron-Electron Interactions in Gap Opening of Zigzag Graphene Nanoribbons. *Nat. Commun.* **2014**, *5*, 4311.
25. Müllen, K. Evolution of Graphene Molecules: Structural and Functional Complexity as Driving Forces Behind Nanoscience. *ACS Nano* **2014**, *8*, 6531–6541.
26. Han, P.; Weiss, P. S. Electronic Substrate-Mediated Interactions. *Surf. Sci. Rep.* **2012**, *67*, 19–81.
27. Yan, L.; Zheng, Y. B.; Zhao, F.; Li, S. J.; Gao, X. F.; Xu, B. Q.; Weiss, P. S.; Zhao, Y. L. Chemistry and Physics of a Single Atomic Layer: Strategies and Challenges for Functionalization of Graphene and Graphene-Based Materials. *Chem. Soc. Rev.* **2012**, *41*, 97–114.
28. Fan, Q.; Gottfried, J. M.; Zhu, J. Surface-Catalyzed C-C Covalent Coupling Strategies toward the Synthesis of Low-Dimensional Carbon-Based Nanostructures. *Acc. Chem. Res.* **2015**, *48*, 2484–2494.
29. Narita, A.; Wang, X.-Y.; Feng, X.; Mullen, K. New Advances in Nanographene Chemistry. *Chem. Soc. Rev.* **2015**, *44*, 6616–6643.
30. Huang, C. H.; Su, C. Y.; Okada, T.; Li, L. J.; Ho, K. I.; Li, P. W.; Chen, I. H.; Chou, C.; Lai, C. S.; Samukawa, S. Ultra-Low-Edge-Defect Graphene Nanoribbons Patterned by Neutral Beam. *Carbon* **2013**, *61*, 229–235.
31. Li, X. S.; Cai, W. W.; An, J. H.; Kim, S.; Nah, J.; Yang, D. X.; Piner, R.; Velamakanni, A.; Jung, I.; Tutuc, E.; *et al.* Large-Area Synthesis of High-Quality and Uniform Graphene Films on Copper Foils. *Science* **2009**, *324*, 1312–1314.
32. Kim, K. S.; Zhao, Y.; Jang, H.; Lee, S. Y.; Kim, J. M.; Kim, K. S.; Ahn, J.-Y.; Kim, P; Choi, J.-Y.; Hong, B. H. Large-Scale Pattern Growth of Graphene Films for Stretchable Transparent Electrodes. *Nature* **2009**, *457*, 706–710.
33. Heimel, G.; Duhm, S.; Salzmann, I.; Gerlach, A.; Strozecka, A.; Niederhausen, J.; Buerker, C.; Hosokai, T.; Fernandez-Torrente, I.; Schulze, G.; *et al.* Charged and Metallic Molecular Monolayers through Surface-Induced Aromatic Stabilization. *Nat. Chem.* **2013**, *5*, 187–194.
34. Treier, M.; Pignedoli, C. A.; Laino, T.; Rieger, R.; Mullen, K.; Passerone, D.; Fasel, R. Surface-Assisted Cyclodehydrogenation Provides a Synthetic Route towards Easily Processable and Chemically Tailored Nanographenes. *Nat. Chem.* **2011**, *3*, 61–67.
35. Yang, R.; Shi, Z.; Zhang, L.; Shi, D.; Zhang, G. Observation of Raman G-Peak Split for Graphene Nanoribbons with Hydrogen-Terminated Zigzag Edges. *Nano Lett.* **2011**, *11*, 4083–4088.
36. Vandescuren, M.; Hermet, P.; Meunier, V.; Henrard, L.; Lambin, P. Theoretical Study of the Vibrational Edge Modes in Graphene Nanoribbons. *Phys. Rev. B: Condens. Matter Mater. Phys.* **2008**, *78*, 195401.
37. Yazyev, O. V.; Louie, S. G. Topological Defects in Graphene: Dislocations and Grain Boundaries. *Phys. Rev. B: Condens. Matter Mater. Phys.* **2010**, *81*, 195420.
38. Gao, L.; Guest, J. R.; Guisinger, N. P. Epitaxial Graphene on Cu(111). *Nano Lett.* **2010**, *10*, 3512–3516.
39. Crommie, M. F.; Lutz, C. P.; Eigler, D. M. Imaging Standing Waves in a 2-Dimensional Electron-Gas. *Nature* **1993**, *363*, 524–527.

40. Hämäläinen, S. K.; Sun, Z.; Boneschanscher, M. P.; Uppstu, A.; Ijäs, M.; Harju, A.; Vanmaekelbergh, D.; Liljeroth, P. Quantum-Confined Electronic States in Atomically Well-Defined Graphene Nanostructures. *Phys. Rev. Lett.* **2011**, *107*, 236803.
41. Phark, S.-h.; Borme, J.; Vanegas, A. L.; Corbetta, M.; Sander, D.; Kirschner, J. Direct Observation of Electron Confinement in Epitaxial Graphene Nanoislands. *ACS Nano* **2011**, *5*, 8162–8166.
42. Hollen, S. M.; Gambrel, G. A.; Tjung, S. J.; Santagata, N. M.; Johnston-Halperin, E.; Gupta, J. A. Modification of Electronic Surface States by Graphene Islands on Cu(111). *Phys. Rev. B: Condens. Matter Mater. Phys.* **2015**, *91*, 195425.
43. Batzill, M. The Surface Science of Graphene: Metal Interfaces, CVD Synthesis, Nanoribbons, Chemical Modifications, and Defects. *Surf. Sci. Rep.* **2012**, *67*, 83–115.
44. Li, Y.; Subramaniam, D.; Atodiresei, N.; Lazic, P.; Caciuc, V.; Pauly, C.; Georgi, A.; Busse, C.; Liebmann, M.; Blugel, S.; *et al.* Absence of Edge States in Covalently Bonded Zigzag Edges of Graphene on Ir(111). *Adv. Mater.* **2013**, *25*, 1967–1972.
45. Merino, P.; Rodrigo, L.; Pinardi, A. L.; Mendez, J.; Lopez, M. F.; Pou, P.; Perez, R.; Gago, J. A. M. Sublattice Localized Electronic States in Atomically Resolved Graphene-Pt(111) Edge-Boundaries. *ACS Nano* **2014**, *8*, 3590–3596.
46. Hanaguri, T. Development of High-Field STM and Its Application to the Study on Magnetically-Tuned Criticality in $Sr_3Ru_2O_7$. *J. Phys.: Conf. Ser.* **2006**, *51*, 514–521.
47. Iwaya, K.; Shimizu, R.; Teramura, A.; Sasaki, S.; Itagaki, T.; Hitosugi, T. Design of an Effective Vibration Isolation System for Measurements Sensitive to Low-Frequency Vibrations. *J. Vac. Sci. Technol., A* **2012**, *30*, 063201.
48. Horcas, I.; Fernandez, R.; Gomez-Rodriguez, J. M.; Colchero, J.; Gomez-Herrero, J.; Baro, A. M. WSXM: A Software for Scanning Probe Microscopy and a Tool for Nanotechnology. *Rev. Sci. Instrum.* **2007**, *78*, 013705.
49. Kresse, G.; Furthmuller, J. Efficient Iterative Schemes for *Ab Initio* Total-Energy Calculations Using a Plane-Wave Basis Set. *Phys. Rev. B: Condens. Matter Mater. Phys.* **1996**, *54*, 11169–11186.
50. Perdew, J. P.; Burke, K.; Ernzerhof, M. Generalized Gradient Approximation Made Simple. *Phys. Rev. Lett.* **1996**, *77*, 3865–3868.